

AN IMPROVED FINITE DIFFERENCE TIME DOMAIN METHOD FOR TWO DIMENSIONAL MAXWELL'S EQUATIONS

TIMOTHY MEAGHER¹, BIN JIANG², PENG JIANG³

ABSTRACT. An efficient finite-difference time-domain (FDTD) algorithm is built to solve the transverse electric 2D Maxwell's equations with inhomogeneous dielectric media where the electric fields are discontinuous across the dielectric interface. The new algorithm is derived based upon the integral version of the Maxwell's equations as well as the relationship between the electric fields across the interface. It is an improvement over the contour-path effective-permittivity algorithm by including some extra terms in the formulas. The scheme is validated in solving the scattering of a dielectric cylinder with exact solution from Mie theory and is then compared with the above contour-path method, the usual staircase and the volume-average method. The numerical results demonstrate that the new algorithm has achieved significant improvement in accuracy over the other methods. Furthermore, the algorithm has a simple structure and can be merged into any existing FDTD software package very easily.

1. INTRODUCTION

The finite-difference time-domain (FDTD) algorithm is one of the most popular numerical methods to solve Maxwell's equations, as proposed by Yee [1]. It is a time marching forward method which easily makes a visual representation of the fields. It also scales very well since the number of computation required is proportional to the size of the model and the method requires no large-scale linear algebra computation [2]. The FDTD method requires a completely structured grid also known as the Yee grid. However, Many real world problems have complicated geometries and numerical inaccuracy happens when the modeled objects do not fit the grid very well.

In this paper, we focus on two-dimensional transverse electric (TE) Maxwell's equation within multiple non-magnetic media where the electric fields are not continuous across the media interface so the numerical schemes need to be designed to take care of such discontinuity. The other case is the transverse magnetic equation where the electric field is always continuous across the media interface and the original algorithm will work as in the homogeneous medium.

The original FDTD algorithm proposed in Yee's paper assigns each of the field component an electric permittivity and a magnetic permeability solely based on the material properties at its location. This is commonly known as the staircasing

¹Department of Mathematical Sciences, University of Nevada, Las Vegas, NV 89154, USA

²Fariborz Maseeh Department of Mathematics and Statistics, Portland State University, Portland OR 97201, USA

³Department of Chemical Engineering, University of Florida, Gainesville, FL 32611, USA

Key words and phrases. finite difference time domain; Maxwell's equations; effective permittivity.

or pixelation method. In general, the staircasing method has an error that scales with $\mathcal{O}(\Delta x^2)$ given a grid size of Δx for cells that are homogenous. However, in cells that contain a medium interface, the local error becomes $\mathcal{O}(1)$. Even though the number of cells that contain an interface is often a small fraction of the total cells, these local errors can cause a rough global error of $\mathcal{O}(\Delta x)$.

Subsequent research in modern optics and electromagnetism dealing with the Maxwell's equations have focused on more and more complex geometries with different materials so that the complicated dielectric tensor can cause serious pixelation issues. In turn, there have been many improvements in FDTD algorithms to overcome these pixelation issues. One way to overcome the pixelation problem is by fitting the mesh to the device, thereby generating the so-called non-orthogonal FDTD [3, 4]. The second method is to refine the Cartesian mesh around the interfaces and is thus called subgridding method [5]. Even though these two methods converge faster than the standard FDTD method, their complexity are larger than original FDTD method and they also have time stability issues.

In order to keep a completely structured grid and maintain all the benefits of FDTD, another method redefines Maxwell's integral equations around the interface of the media. This is known as the effective-permittivity (EP) method. This method uses sub-pixel smoothing techniques to change the permittivities of the field components around the interface to produce better results by taking account of many different factors, such as the interface conditions, permittivities of adjacent field components and so on. The revised effective permittivities smooth out the pixel error. The main benefit of these methods is that there is a negligible increase of the numerical load since all the revised permittivities have been calculated before the main FDTD algorithm loop.

The first method of sub-pixel smoothing is the volume average effective permittivity (V-EP) [6]. This method assigns effective permittivities for all the field components in a cell that contains media interface. The effective permittivities are calculated by taking a weighted average based on how much percent of the volume each medium occupies. This method is simple for implementation and also stabilizes the error fluctuation that occurs in the staircasing method. However, it does not decrease the error rapidly and its error can be worse than staircasing method sometimes due to ignorance of the interface orientation.

The second method proposes dynamic formulas for the EP based on the orientation of the media interface and their expressions are accurate when the interface is perpendicular or parallel to the mesh axes [7, 8, 9]. These EPs improve the accuracy of the FDTD method, while keeping the simple structure of the original algorithm. However, their performance will deteriorate for a curved or flat interface not perpendicular or parallel to the mesh axes.

The third method uses the reflection coefficients to derive effective permittivities and shows the method can also achieve second-order convergence with several special slanted angles between the interface and the Yee grid rather than just orthogonal or parallel to the Yee grid [10, 11]. However, its derivation is quite complicated and has no ways to be extended to arbitrary interfaces.

In a landmark paper [12], Mohammadi et al. proposed the so-called contour-path effective permittivities (CP-EP) method. The CP-EP method first addresses the orthogonal and parallel cases as shown above, then extends the idea to handle with more general geometry. Unlike the previous methods, it could handle arbitrary

boundary with any orientation of the boundary. Compared with traditional stair-casing methods, CE-EP has almost no additional runtime cost since determination of the effective permittivities has been done before the main FDTD loop.

However, we will demonstrate that CP-EP does not incorporate one important term from the interface conditions into the FDTD algorithm. Then we will develop a revised EP algorithm where the missing term will be re-considered in order to produce a more accurate and stable algorithm. Since this method incorporates the boundary conditions very well, it will be denoted as BC-EP.

In fact, such deficiency of CP-EP has also been identified in [13, 14] where effective dielectric permittivity tensors are constructed to take care of both isotropic and anisotropic materials so as to achieve second-order convergence under the open source software MEEP. However, such proposed method which satisfies the interface conditions for electromagnetic fields has been shown to have late-time instabilities, and many possibilities to average the effective dielectric tensor are explored to avoid late time instabilities [15]. Further efforts have been reported in [16] to construct a new second-order scheme by taking the average of eight triplets. Although the new method is highly accurate, its effective dielectric permittivity tensor can still be asymmetric thus unstable for certain conditions. Therefore, the last improvement of the effective dielectric tensor has been given in [17] to make it symmetric and stable. The numerical results show that this scheme gives the best result in general and the error in practice still lies in between first and second-order in most cases.

In the following, we will introduce the new BC-EP method by adding a few terms to the established CP-EP method for the cells around the interface so as to keep the numerical load increase as small as possible and improve the accuracy significantly. Then the numerical tests verify that BC-EP has a much better performance than CP-EP, V-EP and staircasing methods while still maintaining numerical stability. BC-EP has a very simple structure and can be merged into any existing FDTD packages easily, compared with other established FDTD software [14, 17] which can be run only within their framework. Conclusion and some future research consideration will be provided in the end.

2. NEW ALGORITHM DESIGN

In this section, we will propose a new effective permittivity method to solve Maxwell's equations in a domain composed of two different non-magnetic media with different electric permittivities. To simply the algorithm description, we will focus on the most important transverse electric (TE) scenario. That is, $\mathbf{E}(x, y) = E_x \mathbf{i} + E_y \mathbf{j}$ is located in the incident xy-plane while $\mathbf{H}(x, y) = H_z \mathbf{k}$ is along z-axis. Moreover, we restrict the discussion to dielectric and non-magnetic media such that $\mathbf{D}(x, y) = \epsilon \mathbf{E}(x, y)$ and $\mathbf{B}(x, y) = \mathbf{H}(x, y)$ where ϵ stays as a constant in different media and $\epsilon_0 = \mu_0 = 1$. Based on the integral version of the Maxwell's equations, we will derive the new algorithm for any orientation of the interface. This is a significant improvement over all current methods which are only accurate under specific angles between the interface and Cartesian coordinate system, such as parallel or orthogonal to Yee-axis.

As a preliminary step, let us set up the relation of $\mathbf{D}(x, y)$ and $\mathbf{E}(x, y)$ across the interface of these two media. It is well known that $\mathbf{H}(x, y)$ is continuous in the whole domain. Meanwhile, across the media interface, the tangential component $\mathbf{E}_\tau(x, y)$ of the electric field and the normal component $\mathbf{D}_n(x, y)$ of the electric flux

are continuous as well, as shown in Figure 1 where $\mathbf{n} = (n_x, n_y)$ is the outward unit norm vector from region 1. Choose $A \in \Gamma$. $\mathbf{D}_1(A) = (D_{x1}(A), D_{y1}(A))$ and

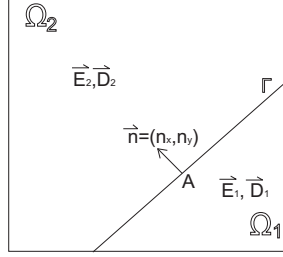


FIGURE 1. Relation of \mathbf{D} and \mathbf{E} across interface Γ

$\mathbf{D}_2(A) = (D_{x2}(A), D_{y2}(A))$ are the electric fluxes at A from different media, and $\mathbf{E}_1(A) = (E_{x1}(A), E_{y1}(A))$ and $\mathbf{E}_2(A) = (E_{x2}(A), E_{y2}(A))$ are the corresponding electric fields.

Suppose $\mathbf{n} = (n_x, n_y)$ is the unit norm vector at A from region 1, then the corresponding tangent unit vector is $\tau = (n_y, -n_x)$. Therefore, we can calculate E_τ and D_n at point A in different regions as follows.

$$E_{\tau_1} = \mathbf{E}_1 \cdot \tau = E_{x1}n_y - E_{y1}n_x \quad (1)$$

$$E_{\tau_2} = \mathbf{E}_2 \cdot \tau = E_{x2}n_y - E_{y2}n_x \quad (2)$$

Meanwhile,

$$D_{n_1} = \epsilon_1 \mathbf{E}_{n_1} = \epsilon_1 E_{x1}n_x + \epsilon_1 E_{y1}n_y \quad (3)$$

$$D_{n_2} = \epsilon_2 \mathbf{E}_{n_2} = \epsilon_2 E_{x2}n_x + \epsilon_2 E_{y2}n_y \quad (4)$$

Based on the fact that $E_{\tau_1} = E_{\tau_2}$ and $D_{n_1} = D_{n_2}$, we have

$$\begin{cases} E_{x1}n_y - E_{y1}n_x &= E_{x2}n_y - E_{y2}n_x \\ \epsilon_1 E_{x1}n_x + \epsilon_1 E_{y1}n_y &= \epsilon_2 E_{x2}n_x + \epsilon_2 E_{y2}n_y \end{cases}$$

Therefore, by using $n_x^2 + n_y^2 = 1$, we get

$$\begin{bmatrix} E_{x1} \\ E_{y1} \end{bmatrix} = \begin{bmatrix} n_y & -n_x \\ \epsilon_1 n_x & \epsilon_1 n_y \end{bmatrix}^{-1} \begin{bmatrix} n_y & -n_x \\ \epsilon_2 n_x & \epsilon_2 n_y \end{bmatrix} \begin{bmatrix} E_{x2} \\ E_{y2} \end{bmatrix}$$

Or

$$\begin{cases} E_{x1} &= (\frac{\epsilon_2}{\epsilon_1} n_x^2 + n_y^2) E_{x2} + (\frac{\epsilon_2}{\epsilon_1} - 1) n_x n_y E_{y2} \\ E_{y1} &= (\frac{\epsilon_2}{\epsilon_1} - 1) n_x n_y E_{x2} + (n_x^2 + \frac{\epsilon_2}{\epsilon_1} n_y^2) E_{y2} \end{cases} \quad (5)$$

Furthermore, by using $\mathbf{D}_i = \epsilon_i \mathbf{E}_i$ at A , we obtain

$$\begin{cases} D_{x1} &= (\frac{\epsilon_1}{\epsilon_2} n_y^2 + n_x^2) D_{x2} + (1 - \frac{\epsilon_1}{\epsilon_2}) n_x n_y D_{y2} \\ D_{y1} &= (1 - \frac{\epsilon_1}{\epsilon_2}) n_x n_y D_{x2} + (\frac{\epsilon_1}{\epsilon_2} n_x^2 + n_y^2) D_{y2} \end{cases} \quad (6)$$

If the interface Γ is parallel or orthogonal to x -axis, either $n_y = 0$ or $n_x = 0$ so $n_x \cdot n_y = 0$. Then the relation (5) involving \mathbf{E}_1 and \mathbf{E}_2 will be simplified such that E_{x1} and E_{y1} will only depend on E_{x2} or E_{y2} , respectively. Same holds for \mathbf{D}_1 and \mathbf{D}_2 in relation (6).

By using (6), we can express D_{x_2} in region 2 based on its neighbor D_{x_1} in region 1 and its corresponding D_{y_2} in the same region 2. Similar formula can also be derived for D_{y_2} based on D_{y_1} and D_{x_2} .

$$D_{x_2} = \frac{\epsilon_2}{\epsilon_2 n_x^2 + \epsilon_1 n_y^2} D_{x_1} + \frac{(\epsilon_1 - \epsilon_2) n_x n_y}{\epsilon_2 n_x^2 + \epsilon_1 n_y^2} D_{y_2} \quad (7)$$

$$D_{y_2} = \frac{(\epsilon_1 - \epsilon_2) n_x n_y}{\epsilon_1 n_x^2 + \epsilon_2 n_y^2} D_{x_2} + \frac{\epsilon_2}{\epsilon_1 n_x^2 + \epsilon_2 n_y^2} D_{y_1} \quad (8)$$

(5) will be used to derive the new scheme for Faraday's law while (7) and (8) will be used to derive the new scheme for Ampere's law.

Now let us express Ampere's law in integral form

$$\frac{\partial}{\partial t} \iint_S \mathbf{D} \cdot \mathbf{n} dS = \oint_{\partial S} \mathbf{H} \cdot d\mathbf{l} \quad (9)$$

and Faraday's law integral form

$$\frac{\partial}{\partial t} \iint_S \mathbf{B} \cdot \mathbf{n} dS = - \oint_{\partial S} \mathbf{E} \cdot d\mathbf{l} \quad (10)$$

Firstly, let us discretize Ampere's law (9) around the interface Γ to update E_x^n and E_y^n as below. To update E_x , we choose S in (9) to be the rectangle in yz -

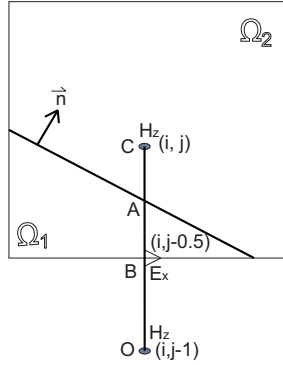


FIGURE 2. Discretization of Ampere's law across Γ

plane whose projection in xy -plane is the line segment OC . Suppose the interface Γ intersect OC at point A and $OA = f$ as in Figure 2. Applying time discretization to Ampere's law along S at time $t_{n+\frac{1}{2}}$ yields

$$\frac{\int_O^C D_{x(i,y)}^{n+1} dy - \int_O^C D_{x(i,y)}^n dy}{\Delta t} = H_{z(i,j)}^{n+\frac{1}{2}} - H_{z(i,j-1)}^{n+\frac{1}{2}} \quad (11)$$

Based on formula (7), we can compute the integrals of left hand side as follows. From now on, all the higher-order terms of dx and dy are ignored for the clarification

of the formulas.

$$\begin{aligned}
\int_O^C D_{x(i,y)}^{n+1} dy &= \int_O^A D_{x(i,y)}^{n+1} dy + \int_A^C D_{x(i,y)}^{n+1} dy \\
&= f D_{x(i,j-\frac{1}{2})}^{n+1} + (\Delta y - f) D_{x(A,\Omega_2)}^{n+1} \\
&= f D_{x(i,j-\frac{1}{2})}^{n+1} + (\Delta y - f) \left[\frac{\epsilon_2}{\epsilon_2 n_x^2 + \epsilon_1 n_y^2} D_{x(A,\Omega_1)}^{n+1} + \frac{(\epsilon_1 - \epsilon_2) n_x n_y}{\epsilon_2 n_x^2 + \epsilon_1 n_y^2} D_{y(A,\Omega_2)}^{n+1} \right] \\
&= \frac{f(\epsilon_2 n_x^2 + \epsilon_1 n_y^2) + (\Delta y - f) \epsilon_2}{\epsilon_2 n_x^2 + \epsilon_1 n_y^2} D_{x(i,j-\frac{1}{2})}^{n+1} + \frac{(\epsilon_1 - \epsilon_2) n_x n_y}{\epsilon_2 n_x^2 + \epsilon_1 n_y^2} (\Delta y - f) D_{y(C)}^{n+1}
\end{aligned} \tag{12}$$

Similarly,

$$\begin{aligned}
\int_O^C D_{x(i,y)}^n dy &= \frac{f(\epsilon_2 n_x^2 + \epsilon_1 n_y^2) + (\Delta y - f) \epsilon_2}{\epsilon_2 n_x^2 + \epsilon_1 n_y^2} D_{x(i,j-\frac{1}{2})}^n \\
&\quad + \frac{(\epsilon_1 - \epsilon_2) n_x n_y}{\epsilon_2 n_x^2 + \epsilon_1 n_y^2} (\Delta y - f) D_{y(C)}^n
\end{aligned} \tag{13}$$

Furthermore,

$$\begin{aligned}
D_{y(C)}^{n+1} &= D_{y(C)}^n + \frac{\partial D_y}{\partial t} \Big|_C^{t_n} \cdot \Delta t \\
&= D_{y(C)}^n - \frac{\partial H_z}{\partial x} \Big|_C^{t_{n+\frac{1}{2}}} \cdot \Delta t \\
&= D_{y(C)}^n - \left(\frac{H_{z(i,j)}^{n+\frac{1}{2}} - H_{z(i-1,j)}^{n+\frac{1}{2}}}{\Delta x} \right) \Delta t
\end{aligned} \tag{14}$$

By putting (12), (13) and (14) into (11), we obtain

$$\begin{aligned}
\frac{f(\epsilon_2 n_x^2 + \epsilon_1 n_y^2) + (\Delta y - f) \epsilon_2}{\epsilon_2 n_x^2 + \epsilon_1 n_y^2} \left(D_{x(i,j-\frac{1}{2})}^{n+1} - D_{x(i,j-\frac{1}{2})}^n \right) &= \Delta t \left(H_{z(i,j)}^{n+\frac{1}{2}} - H_{z(i,j-1)}^{n+\frac{1}{2}} \right) \\
&\quad + \frac{\Delta t}{\Delta x} \frac{(\epsilon_1 - \epsilon_2) n_x n_y}{\epsilon_2 n_x^2 + \epsilon_1 n_y^2} (\Delta y - f) \left(H_{z(i,j)}^{n+\frac{1}{2}} - H_{z(i-1,j)}^{n+\frac{1}{2}} \right)
\end{aligned} \tag{15}$$

which, based on $D_x = \epsilon_1 E_x$ in Ω_1 , becomes

$$\begin{aligned}
E_{x(i,j-\frac{1}{2})}^{n+1} &= E_{x(i,j-\frac{1}{2})}^n + \Delta t \frac{\frac{\epsilon_2}{\epsilon_1} n_x^2 + n_y^2}{f(\epsilon_2 n_x^2 + \epsilon_1 n_y^2) + (\Delta y - f) \epsilon_2} \left(H_{z(i,j)}^{n+\frac{1}{2}} - H_{z(i,j-1)}^{n+\frac{1}{2}} \right) \\
&\quad + \frac{\Delta t}{\Delta x} \frac{(\Delta y - f) (1 - \frac{\epsilon_2}{\epsilon_1}) n_x n_y}{f(\epsilon_2 n_x^2 + \epsilon_1 n_y^2) + (\Delta y - f) \epsilon_2} \left(H_{z(i,j)}^{n+\frac{1}{2}} - H_{z(i-1,j)}^{n+\frac{1}{2}} \right)
\end{aligned} \tag{16}$$

which shows improved discretization of Ampere's law for updating E_x .

It should also be noted that the last term on the right hand side of (16) have been ignored by CP-EP for algorithm simplification but it indeed provides necessary corrections for the interface conditions across multiple media. Furthermore, the numerical tests have also verified that in order to make the algorithm for Ampere's Law more accurate, these two H_z values in the last term should stay close to the interface. That is, if the normal direction of the interface n satisfies $n_x \cdot n_y > 0$ as shown in Figure 2, we use $(H_{z(i,j)}^{n+\frac{1}{2}} - H_{z(i-1,j)}^{n+\frac{1}{2}})$ since these two H_z points are closer

to the interface, while for the other $n_x \cdot n_y \leq 0$ case, we use $(H_{z(i+1,j)}^{n+\frac{1}{2}} - H_{z(i,j)}^{n+\frac{1}{2}})$ in (16) instead since these two H_z nodes are closer to the interface than the other pair. This improvement is feasible since H_z is continuous across the interface.

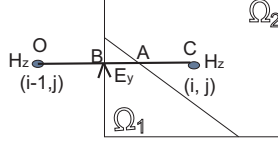


FIGURE 3. Discretization of the integral along OC

Similarly, update of E_y at point $B = (i - \frac{1}{2}, j)$ by Ampere's law (9) can be taken care analogously as shown in Figure 3, where the interface Γ intersects the line segment OC , projection of S at xy -plane, at A . Let $OA = d$. By repeating the same procedure as above while based on formula (8), we can also obtain the discretization of Ampere's law for E_y as below:

$$E_{y(i,j-\frac{1}{2})}^{n+1} = E_{y(i,j-\frac{1}{2})}^n + \Delta t \frac{\frac{\epsilon_2}{\epsilon_1} n_y^2 + n_x^2}{d(\epsilon_1 n_x^2 + \epsilon_2 n_y^2) + (\Delta x - d)\epsilon_2} \left(H_{z(i-1,j)}^{n+\frac{1}{2}} - H_{z(i,j)}^{n+\frac{1}{2}} \right) + \frac{\Delta t}{\Delta y} \frac{(\Delta x - d)(1 - \frac{\epsilon_2}{\epsilon_1}) n_x n_y}{d(\epsilon_1 n_x^2 + \epsilon_2 n_y^2) + (\Delta x - d)\epsilon_2} \left(H_{z(i,j-1)}^{n+\frac{1}{2}} - H_{z(i,j)}^{n+\frac{1}{2}} \right) \quad (17)$$

where $(H_{z(i,j-1)}^{n+\frac{1}{2}} - H_{z(i,j)}^{n+\frac{1}{2}})$ in the last term will be replaced by $(H_{z(i,j)}^{n+\frac{1}{2}} - H_{z(i,j+1)}^{n+\frac{1}{2}})$ when $n_x \cdot n_y \leq 0$ holds.

Secondly, let's discretize Faraday's law (10) around the interface Γ . We choose

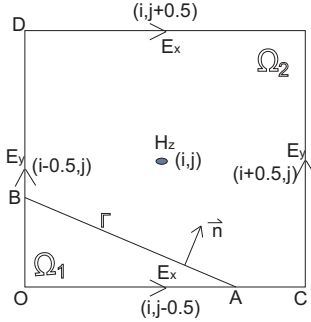


FIGURE 4. Discretization of Faraday's law across Γ

S to be the rectangle centered at (i, j) . If the medium interface Γ does not cut through interior of S , the standard Yee scheme should apply without modification. So we only consider the case where Γ intersects with S . It's obvious that Γ will only intersect with at most two sides, e.g. the bottom and left side as in Figure 4. All other cases can be handled in the same way. Similarly as for Ampere's law, all the higher-order terms of dx and dy are ignored for the clarification of the formulas. Discretization of the left hand side term of (10) at the time t_n via finite difference

scheme yields

$$\frac{\iint_S \mathbf{H}^{n+\frac{1}{2}} \cdot \mathbf{n} dS - \iint_S \mathbf{H}^{n-\frac{1}{2}} \cdot \mathbf{n} dS}{\Delta t} = - \oint_{\partial S} \mathbf{E}^n \cdot d\mathbf{l}$$

or

$$\iint_S \mathbf{H}^{n+\frac{1}{2}} \cdot \mathbf{n} dS = \iint_S \mathbf{H}^{n-\frac{1}{2}} \cdot \mathbf{n} dS - \Delta t \oint_{\partial S} \mathbf{E}^n \cdot d\mathbf{l} \quad (18)$$

since \mathbf{H} is always perpendicular to the incident xy -plane and so is always continuous across the interface, then by using midpoint rule,

$$\iint_S \mathbf{H}^{n+\frac{1}{2}} \cdot \mathbf{n} dS = H_{z(i,j)}^{n+\frac{1}{2}} \Delta x \Delta y \quad (19)$$

$$\iint_S \mathbf{H}^{n-\frac{1}{2}} \cdot \mathbf{n} dS = H_{z(i,j)}^{n-\frac{1}{2}} \Delta x \Delta y \quad (20)$$

However, the situation for \mathbf{E} is much more complicated. In Figure 4, the line integral of \mathbf{E}^n along the right and top sides can be handled as Standard Yee scheme since they are completely inside Ω_2 . But the line integrals along the bottom and left sides need to be handled separately.

$$\begin{aligned} \oint_{\partial S} \mathbf{E}^n \cdot d\mathbf{l} &= \int_{bottom} \mathbf{E}^n \cdot d\mathbf{l} + \int_{left} \mathbf{E}^n \cdot d\mathbf{l} \\ &+ \int_{(j-\frac{1}{2})\Delta y}^{(j+\frac{1}{2})\Delta y} E_{(i+\frac{1}{2},y)}^n dy - \int_{(i-\frac{1}{2})\Delta x}^{(i+\frac{1}{2})\Delta x} E_{(x,j+\frac{1}{2})}^n dx \\ &= \int_O^C E_{(x,j-\frac{1}{2})}^n dx - \int_O^D E_{(i-\frac{1}{2},y)}^n dy + E_{y(i+\frac{1}{2},j)}^n \Delta y - E_{x(i,j+\frac{1}{2})}^n \Delta x \end{aligned} \quad (21)$$

Suppose the portion OA of the bottom side in Ω_1 has length d , and the portion OB of the left side in Ω_1 has length f as in Figure 4, then the first two terms on the right hand side of (21) can be handled as below. For the first term on the right hand side of (21), we have

$$\begin{aligned} \int_O^C E_{(x,j-\frac{1}{2})}^n dx &= \int_O^A E_{(x,j-\frac{1}{2})}^n dx + \int_A^C E_{(x,j-\frac{1}{2})}^n dx \\ &= E_{x(i,j-\frac{1}{2})}^n \cdot d + E_x|_{A,\Omega_2} \cdot (\Delta x - d) \end{aligned} \quad (22)$$

By using formula (5) with Ω_1 and Ω_2 interchanged, we have

$$E_x|_{A,\Omega_2} = (\frac{\epsilon_1}{\epsilon_2} n_x^2 + n_y^2) E_x|_{A,\Omega_1} + (\frac{\epsilon_1}{\epsilon_2} - 1) n_x n_y E_y|_{A,\Omega_1} \quad (23)$$

Putting it into (22) yields

$$\begin{aligned} \int_O^C E_{(x,j-\frac{1}{2})}^n dx &= E_{x(i,j-\frac{1}{2})}^n \cdot d + (\frac{\epsilon_1}{\epsilon_2} n_x^2 + n_y^2) (\Delta x - d) E_x|_{A,\Omega_1} \\ &+ (\frac{\epsilon_1}{\epsilon_2} - 1) n_x n_y (\Delta x - d) E_y|_{A,\Omega_1} \\ &= [d + (\Delta x - d) (\frac{\epsilon_1}{\epsilon_2} n_x^2 + n_y^2)] E_{x(i,j-\frac{1}{2})}^n \\ &+ (\frac{\epsilon_1}{\epsilon_2} - 1) n_x n_y (\Delta x - d) E_{y(i,j-\frac{1}{2})}^n \end{aligned} \quad (24)$$

where $E_{y(i,j-\frac{1}{2})}^n$ is the value of E_y evaluated at point $(i, j - \frac{1}{2})$ in Ω_1 . However, only E_x instead of E_y is calculated at the mesh point $(i, j - \frac{1}{2})$. Therefore, we will

take the average value of E_y^n at the neighboring pair of mesh points $(i - \frac{1}{2}, j - 1)$ and $(i + \frac{1}{2}, j)$ if they are both located within Ω_1 , or take the average value of E_y^n at the other neighboring pair mesh points $(i - \frac{1}{2}, j)$ and $(i + \frac{1}{2}, j - 1)$ if they are both located within Ω_1 . If none of the pairs are located within Ω_1 , this term will be set to zero as in CP-EP. Therefore, BC-EP will try to make corrections for the missing terms in CP-EP if possible.

Similarly, we can calculate the second term on the right hand side of (21). Since the E_y node $(i - \frac{1}{2}, j)$ is located within Ω_2 instead of Ω_1 , so the new \mathbf{n} should be negative of the old \mathbf{n} used above. Therefore, applying integration midpoint rule, Taylor expansion and formula (5) where (n_x, n_y) replaced by $(-n_x, -n_y)$ and ϵ_1, ϵ_2 interchanged, we have

$$\begin{aligned} \int_0^D E_{x(i-\frac{1}{2},y)}^n dy &= [f(n_x^2 + \frac{\epsilon_2}{\epsilon_1} n_y^2) + (\Delta y - f)] E_{y(i-\frac{1}{2},j)}^n \\ &\quad + (\frac{\epsilon_2}{\epsilon_1} - 1) n_x n_y f E_{x(i-\frac{1}{2},j)}^n \end{aligned} \quad (25)$$

when $E_{x(i-\frac{1}{2},j)}^n$ will be taken care similarly as $E_{y(i,j-\frac{1}{2})}^n$ from the first term. By putting (24), (25) into (21), we get

$$\begin{aligned} \oint_{\partial S} \mathbf{E}^n \cdot d\mathbf{l} &= [d + (\Delta x - d)(\frac{\epsilon_1}{\epsilon_2} n_x^2 + n_y^2)] E_{x(i,j-\frac{1}{2})}^n + E_{y(i+\frac{1}{2},j)}^n \Delta y - E_{x(i,j+\frac{1}{2})}^n \Delta x \\ &\quad - [f(n_x^2 + \frac{\epsilon_2}{\epsilon_1} n_y^2) + (\Delta y - f)] E_{y(i-\frac{1}{2},j)}^n + (\frac{\epsilon_1}{\epsilon_2} - 1) n_x n_y (\Delta x - d) E_{y(i,j-\frac{1}{2})}^n \\ &\quad - (\frac{\epsilon_2}{\epsilon_1} - 1) n_x n_y f E_{x(i-\frac{1}{2},j)}^n \end{aligned} \quad (26)$$

Finally, by putting (19), (20) and (26) into (18) and dividing both sides by $\Delta x \Delta y$, we obtain the new discretization of Faraday's law:

$$\begin{aligned} H_{z(i,j)}^{n+\frac{1}{2}} &= H_{z(i,j)}^{n-\frac{1}{2}} - \frac{\Delta t}{\Delta x \Delta y} \{ [d + (\Delta x - d)(\frac{\epsilon_1}{\epsilon_2} n_x^2 + n_y^2)] E_{x(i,j-\frac{1}{2})}^n + E_{y(i+\frac{1}{2},j)}^n \Delta y \\ &\quad - E_{x(i,j+\frac{1}{2})}^n \Delta x - [f(n_x^2 + \frac{\epsilon_2}{\epsilon_1} n_y^2) + (\Delta y - f)] E_{y(i-\frac{1}{2},j)}^n \\ &\quad + (\frac{\epsilon_1}{\epsilon_2} - 1) n_x n_y (\Delta x - d) E_{y(i,j-\frac{1}{2})}^n - (\frac{\epsilon_2}{\epsilon_1} - 1) n_x n_y f E_{x(i-\frac{1}{2},j)}^n \} \end{aligned} \quad (27)$$

where the last two terms are expressed by

$$E_{y(i,j-\frac{1}{2})}^n = \begin{cases} \frac{1}{2}(E_{y(i-\frac{1}{2},j-1)}^n + E_{y(i+\frac{1}{2},j)}^n) & \text{if } (i - \frac{1}{2}, j - 1) \in \Omega_1, \quad (i + \frac{1}{2}, j) \in \Omega_1 \\ \frac{1}{2}(E_{y(i-\frac{1}{2},j)}^n + E_{y(i+\frac{1}{2},j-1)}^n) & \text{if } (i - \frac{1}{2}, j) \in \Omega_1, \quad (i + \frac{1}{2}, j - 1) \in \Omega_1 \\ 0 & \text{otherwise} \end{cases}$$

and

$$E_{x(i-\frac{1}{2},j)}^n = \begin{cases} \frac{1}{2}(E_{x(i-1,j-\frac{1}{2})}^n + E_{x(i,j+\frac{1}{2})}^n) & \text{if } (i - 1, j - \frac{1}{2}) \in \Omega_2, \quad (i, j + \frac{1}{2}) \in \Omega_2 \\ \frac{1}{2}(E_{x(i-1,j+\frac{1}{2})}^n + E_{x(i,j-\frac{1}{2})}^n) & \text{if } (i - 1, j + \frac{1}{2}) \in \Omega_2, \quad (i, j - \frac{1}{2}) \in \Omega_2 \\ 0 & \text{otherwise} \end{cases}$$

If we set $\epsilon_1 = \epsilon_2$ in the new algorithm (16), (17) for Ampere's law and (27) for Faraday's law, we can retrieve the standard FDTD scheme in homogeneous medium. Therefore, BC-EP is a simple extension of the original schemes in order to take care of the media interface. Meanwhile, the extra terms added in the formulas will greatly improve the accuracy compared with CP-EP. Furthermore, BC-EP has a

very simple structure and can be merged into any FDTD software by just revising the effective permittivities and adding some extra terms when necessary.

It should be mentioned that due to complicated expressions of those ignored higher-order terms in the newly derived formulas, it is difficult to demonstrate the convergence order of BC-EP theoretically. However, subsequent numerical results will show that BC-EP can achieve the highest convergence (close to second order) compared with other methods. Another point is that it is still an open challenge to accurately handle objects with sharp corners, where the resulting field singularities are known to degrade the accuracy of all numerical schemes [14]. Therefore, just as other methods, BC-EP performs well for straight or curved interfaces instead of interfaces with corners.

3. NUMERICAL RESULTS

In this section, we will demonstrate convergence order and stability of BC-EP numerically. To accomplish this task, we implement the algorithm to solve the Maxwell's equations on a dielectric cylinder, together with the staircasing, V-EP, and CP-EP methods. All the implementations are set up for the 2D FDTD TE case. The total scattering cross sections (SCS) are calculated by all four methods and then compared with the well-known analytic solution by Mie Theory [18] so as to measure the accuracy of each method.

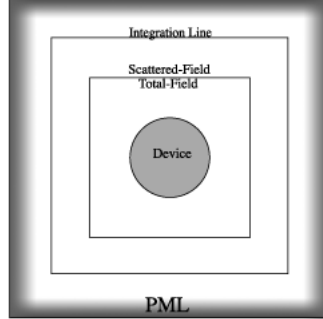


FIGURE 5. The numerical test setup using a dielectric cylinder, giving enough space for the total-field/scattered-field and integration line before the PML

The dielectric cylinder is simulated in an area that is 10 times the radius of the cylinder plus some extra space for PML condition. The cylinder is centered at $((\frac{N_x}{2} + 0.5)\Delta x, (\frac{N_y}{2} + 0.5)\Delta y)$ where N_x and N_y are the number of the cells along the x and y directions, Δx and Δy are the horizontal and vertical mesh sizes of each cell as seen in Figure 5. We run the test for two cases: one case for a larger cylinder with radius $r = 400\text{nm}$ and another case for a smaller cylinder with $r = 150\text{nm}$. The total-field/scattered-field line is three times the length of the cylinder radius r away from the center, and the integration line for calculating SCS is four times r away from the center, while the PML starts at five times r away from the center.

The source wave is a planar wave in the E_y direction with a Gaussian envelope $e^{\frac{-(t-t_0)^2}{2} \cdot \frac{1}{2\pi(c/\lambda_0 - c/\lambda_1)^2}} \cdot \cos(2\pi ct)$, where t_0 is six times Δt , c is speed of light in a vacuum, and $[\lambda_0, \lambda_1]$ is the testing range of wavelengths. In our simulation, we calculate SCS for 601 wavelengths ranging from $\lambda_0 = 400\text{nm}$ to $\lambda_1 = 1000\text{nm}$ of visual light spectrum with equal distance. Fast Fourier transform (FFT) is then applied to transform the electric and magnetic fields from spatial domain into light frequency domain so as to calculate SCS over all related wavelengths.

We use square unit cells with $\Delta x = \Delta y$ to simplify the simulation. The time step is set to $\Delta t = \frac{S\Delta x}{c}$ where $S = \frac{0.98}{\sqrt{3}}$ to ensure stability [2]. Also for stability concerns, Δx were chosen to divide the smallest tested wave length ($\lambda_0 = 400\text{nm}$) by at least twenty times. The total SCS is calculated by using the Poynting Vector along with the integration line as seen in Figure 5. Meanwhile, Mie theory is used to calculate the true value of total SCS for each wavelength. The number of iterations for the main FDTD loop is set large enough in order to give enough time for the electric and magnetic waves to leave the simulated area for stable SCS calculation.

Firstly, we investigate the accuracy and the convergence order of BC-EP and compare it with other similar methods. We test all the methods for a circular cylinder with radius $r = 400\text{nm}$ and permittivity $\epsilon = 3$. The background media is always set as air with $\epsilon = 1$. The mesh size is originally set to $\Delta x = \Delta y = 10\text{nm}$. Each method has been run to calculate the total SCS with different mesh sizes. As seen in Figure 6, the relative errors between the numerical values from all methods and the true solution are quite small. But we can still see that BC-EP has the smallest error while V-EP has the largest error. Meanwhile, for each mesh size Δx , the average relative error of SCS is calculated among all the wavelengths for each method. In order to observe the error convergence order clearly, the average relative errors versus the mesh sizes are converted into a log scale where N_λ denotes the log of the number of mesh points for the radius of the cylinder, as seen in Figure 7.

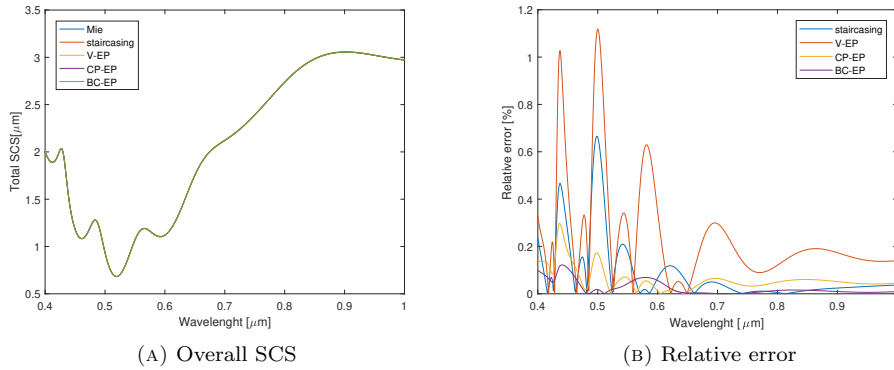


FIGURE 6. Total SCS calculation of a cylinder, $\epsilon = 3$ and radius $r = 400\text{nm}$. The grid size is $\Delta x = \Delta y = 2.8\text{nm}$.

This whole process is then repeated for other larger permittivity values $\epsilon = 6, 10$. The numerical results are reported in Figure 8 and Figure 9 for $\epsilon = 6$, and in Figure 10 and Figure 11 for $\epsilon = 10$. Other ϵ values have similar outcomes.

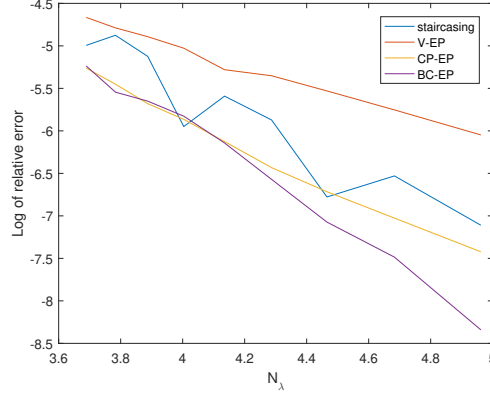


FIGURE 7. The average relative error of a cylinder in log scale, $\epsilon = 3$ and radius $r = 400\text{nm}$. $N_\lambda = \log(\frac{400\text{nm}}{\Delta x})$.

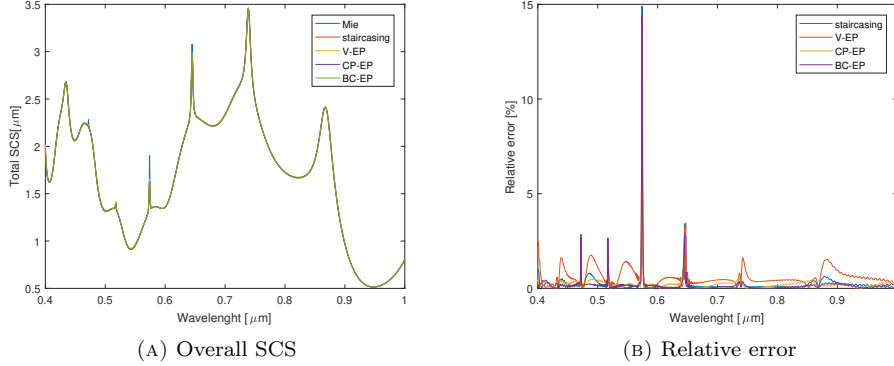


FIGURE 8. Total SCS calculation of a cylinder, $\epsilon = 6$ and radius $r = 400\text{nm}$. The grid size is $\Delta x = \Delta y = 2.8\text{nm}$.

It can be seen that BC-EP gives the least amount of error for most cases, followed by CP-EP. Staircasing results are quite erratic and its error doesn't go down in a uniform manner due to random nature of some mesh sizes conforming with the cylinder better than others. V-EP has the worst error but gives a uniform error decrease with smaller mesh sizes, and thus gives more consistent results over staircasing.

To further investigate the order of convergence of all the methods, we estimate the convergence order by computing the slopes from the log figures for all the given permittivity. Table 1 shows BC-EP converges significantly faster than all the other methods. It approaches second-order in most cases. CP-EP is the second in terms of convergence order and outperforms both staircasing and V-EP as demonstrated in [12] already.

To complete the final evaluation of the performance for all the methods, the whole test suite is then repeated for another circular cylinder with smaller radius

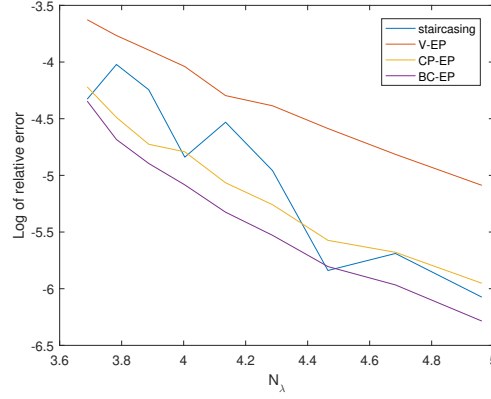


FIGURE 9. The average relative error of a cylinder in log scale, $\epsilon = 6$ and radius $r = 400\text{nm}$. $N_\lambda = \log(\frac{400\text{nm}}{\Delta x})$.

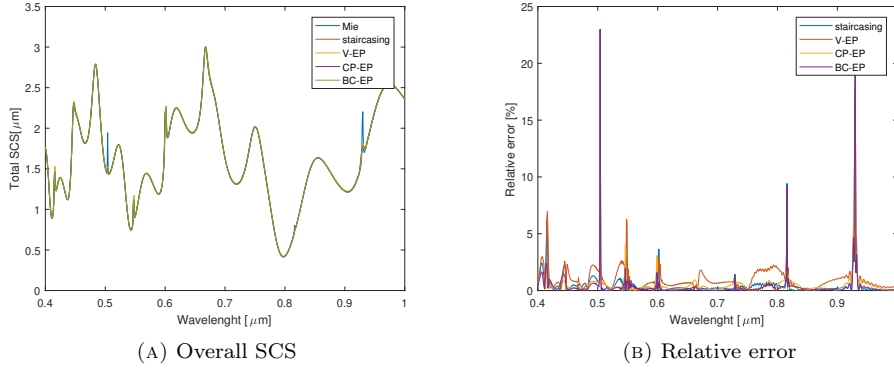


FIGURE 10. Total SCS calculation of a cylinder, $\epsilon = 10$ and radius $r = 400\text{nm}$. The grid size is $\Delta x = \Delta y = 2.8\text{nm}$.

Permittivity	Staircasing	V-EP	CP-EP	BC-EP
$\epsilon = 3$	1.6621	1.0860	1.6977	2.4386
$\epsilon = 4$	1.0700	1.0850	1.4560	1.9251
$\epsilon = 5$	1.2160	1.1294	1.5267	1.6974
$\epsilon = 6$	1.3723	1.1476	1.3607	1.5247
$\epsilon = 7$	1.4322	1.1834	1.3800	1.6014
$\epsilon = 8$	1.4283	1.1860	1.3564	1.6423
$\epsilon = 9$	1.4867	1.2262	1.4333	1.6837
$\epsilon = 10$	1.6172	1.3183	1.5323	1.8006

TABLE 1. Order of convergence for each FDTD algorithm and for each given permittivity in a cylinder of $r = 400\text{nm}$.

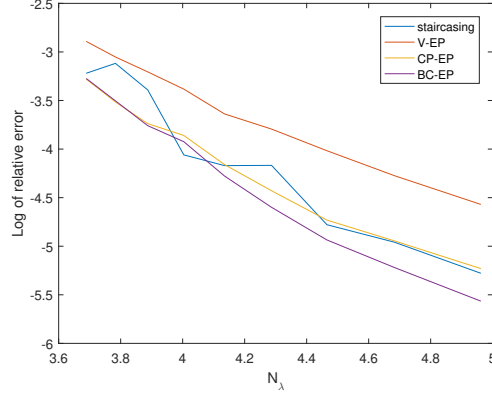


FIGURE 11. The average relative error of a cylinder in log scale, $\epsilon = 10$ and radius $r = 400\text{nm}$. $N_\lambda = \log(\frac{400\text{nm}}{\Delta x})$.

$r = 150\text{nm}$. All the results are very similar and for brevity, we only report the case of $\epsilon = 6$, as seen in Figure 12 and Figure 13. It can be seen that BC-EP has a higher convergence order than others. To be more specific, BC-EP, CP-EP, Staircasing and V-EP have the order of convergence 1.4005, 0.92869, 0.92802 and 1.0059, respectively, based on Figure 13.

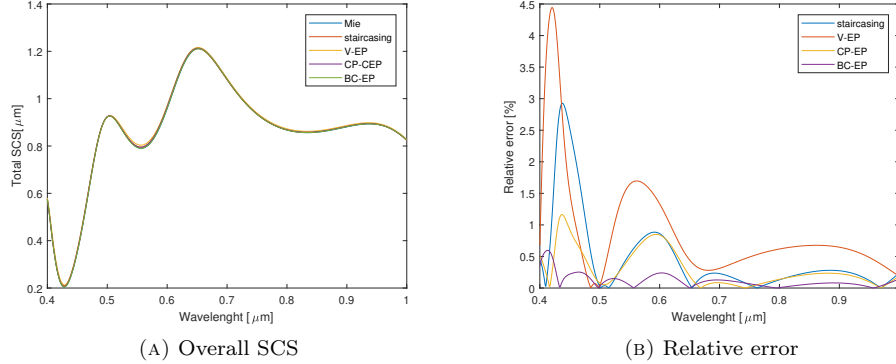


FIGURE 12. Total SCS calculation of a cylinder, $\epsilon = 6$ and radius $r = 150\text{nm}$. The grid size is $\Delta x = \Delta y = 2.8\text{nm}$.

Therefore, BC-EP is more accurate and converges faster than the other three popular FDTD methods.

Secondly, we investigate the stability of BC-EP since the stability of other methods have been demonstrated in the literature. The algorithm has been run for 200,000 iterations under FDTD main loop which is long enough for the electric and magnetic waves completely leave the region as seen in Figure 14. This process has been repeated for $\epsilon = 3, 10, 30$ and for mesh size $\Delta x = 10\text{nm}, 7.3\text{nm}, 4.6\text{nm}$, and 2.8nm . At every 2,000 iterations, a calculation of the SCS for all 601 wavelengths

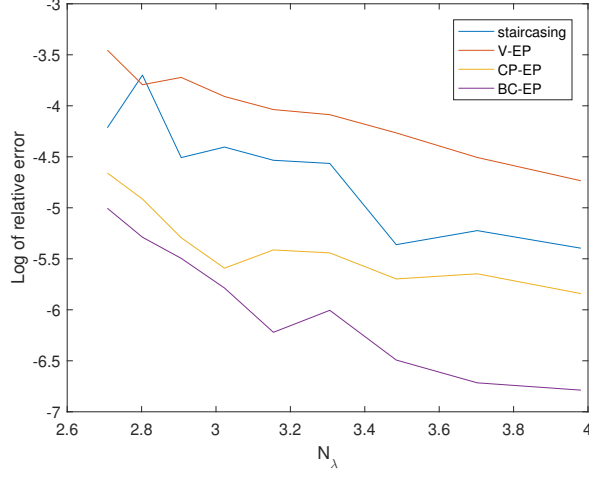


FIGURE 13. The average relative error of a cylinder in log scale, $\epsilon = 6$ and radius $r = 150\text{nm}$. $N_\lambda = \log(\frac{150\text{nm}}{\Delta x})$.

is conducted. Then the average relative error between the calculated SCS at that iteration and the exact SCS over those wavelengths is calculated. We observe that the result are very similar for different ϵ and different Δx in the sense that the relative errors drop down to zero very quickly. This shows that there is no electromagnetic power left in the region and the fields return back to zero as expected, meaning no late time instability even at very high contrast.

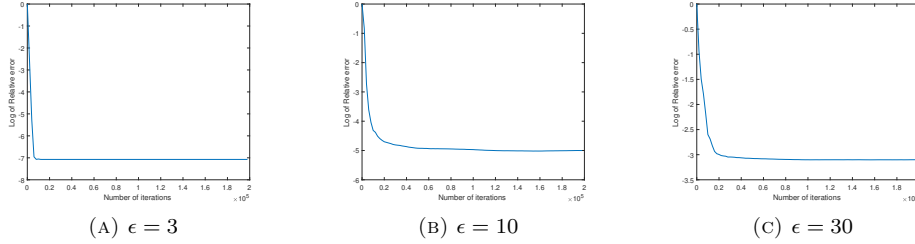


FIGURE 14. Relative error in log format for the SCS calculation at a given iteration with $r = 400\text{nm}$. $\Delta x = \Delta y = 4.6\text{nm}$.

4. CONCLUSIONS AND FUTURE RESEARCH

We have built a new BC-EP method for the challenging two-dimensional transverse electric Maxwell's equations involving multiple dielectric media. Based on a relation for the electric fields across the dielectric media interface and the integral version of the Maxwell's equations, we derived this method which represents Maxwell's equations accurately while the previous numerical methods skipped some terms from the boundary conditions for the purpose of algorithm simplification. We

then apply BC-EP together with three other popular FDTD methods, BC-EP, staircase and V-EP, to solve a numerical example of a dielectric cylinder with given analytic solution. The numerical results clearly demonstrated that it always achieves the highest convergence (close to second order) compared with other methods. The stability of BC-EP has also been verified numerically. Due to its simplicity, BC-EP can be merged into other FDTD software packages easily.

Our next research consideration is to extend BC-EP to solve two-dimensional Maxwell's equations involving multiple dispersive media. Numerical performance comparison of this method with other reported dispersive methods ([19, 20, 21]) will be provided.

REFERENCES

- [1] Kane Yee, *Numerical Solution of Initial Boundary Value Problems Involving Maxwell's Equations in Isotropic Media*, IEEE Transactions on Antennas and Propagation **14**, 302–307 (1966).
- [2] Allen Taflov, Susan Hagness, *Computational Electrodynamics: The Finite-Difference Time-Domain Method*, 3rd Ed. (Artech House, 2005).
- [3] P.H. Harms, J.-F. Lee, R. Mittra, *A Study of the Nonorthogonal FDTD Method Versus the Conventional FDTD Technique for Computing Resonant Frequencies of Cylindrical Cavities*, IEEE Transactions on Microwave Theory and Techniques **40**, 741–746 (1992).
- [4] Jinjie Liu, Moysey Brio, Jerome V. Moloney, *Overlapping Yee FDTD Method on Nonorthogonal Grids*, Journal of Scientific Computing, **39**, 129–143 (2009).
- [5] S.S. Zivanovic, K.S. Yee, K.K. Mei, *A Subgridding Method for the Time-Domain Finite-Difference Method to Solve Maxwell's Equations*, IEEE Transactions on Microwave Theory and Techniques (39), 471–479 (1991).
- [6] Supriyo Dey, Raj Mittra, *A conformal finite-difference time-domain technique for modeling cylindrical dielectric resonators*, IEEE Transactions on Microwave Theory and Techniques **47**, 1737–1739 (1999).
- [7] Noriaki Kaneda, Bijan Houshmand, Tatsuo Itoh, *FDTD Analysis of Dielectric Resonators with Curved Surfaces*, IEEE Transactions on Microwave Theory and Technique **45**, 1645–1648 (1997).
- [8] Kyu-pyung Hwang, Andreas Cangellaris, *Effective Permittivities for Second-Order Accurate FDTD Equations at Dielectric Interfaces*, IEEE Microwave and Wireless Components Letters **60**, 5259–5267 (2012).
- [9] Dauh-churn Liu, Hung-chun Chang, *The Second-order Condition of FDTD Method at Sloped Dielectric Interfaces by Averaging the Permittivities along Surface Normal*, IEEE Transactions on Antennas and Propagation **37**, 4802–4804 (2012).
- [10] T. Hirono, Y. Shibata, W. Lui, S. Seki, Y. Yoshikuni, *The Second-Order Condition for the Dielectric Interface Orthogonal to the Yee-Lattice Axis in the FDTD Scheme*, IEEE Microwave and Guided Wave Letters **10**, 359–361 (2000).
- [11] Takuo Hirono, Yuzo Yoshikuni, Takayuki Yamanaka, *Effective permittivities with exact second-order accuracy at inclined dielectric interface for the two-dimensional finite-difference time-domain method*, Applied optics **49**, 1080–1096 (2010).
- [12] Ahmad Mohammadi, Hamid Nadgaran, Mario Agio, *Contour-path effective permittivities for the two-dimensional finite-difference time-domain method*, Optics Express **13**, 10367–10381 (2005).
- [13] A. Farjadpour, David Roundy, Alejandro Rodriguez, M. Ibanescu, Peter Bermel, J.D. Joannopoulos, Steven Johnson, G.W. Burr, *Improving accuracy by subpixel smoothing in the finite-difference time domain*, Optics letters **31**, 2972–2974 (2006).
- [14] Ardavan Oskooi, Chris Kottke, Steven Johnson, *Accurate finite-difference time-domain simulation of anisotropic media by subpixel smoothing*, Optics letters **34**, 2778–2780 (2009).
- [15] Gregory Werner, John Cary, *A stable FDTD algorithm for non-diagonal, anisotropic dielectrics*, Journal of Computational Physics **226**, 1085–1101 (2007).

- [16] Carl Bauer, Gregory Werner, John Cary, *A second-order 3D electromagnetics algorithm for curved interfaces between anisotropic dielectrics on a Yee mesh*, Journal of Computational Physics **230**, 2060–2075 (2011).
- [17] Gregory Werner, Carl Bauer, John Cary, *A more accurate, stable, FDTD algorithm for electromagnetics in anisotropic dielectrics*, Journal of Computational Physics **255**, 436–455 (2013).
- [18] Craig Bohren, Donald Huffman, *Absorption and scattering of light by small particles*, (John Wiley and Sons, 1983).
- [19] Ahmad Mohammadi, Tahmineh Jalali, Mario Agio, *Dispersive contour-path algorithm for the two-dimensional finite-difference time-domain method*, Optics Express **16**, 7397–7406 (2008).
- [20] Jinjie Liu, Moysey Brio, Jerome V. Moloney, *Subpixel smoothing finite-difference time-domain method for material interface between dielectric and dispersive media*, Optics letters **37**, 4802–4804 (2012).
- [21] Duc Duy Nguyen, Shan Zhao, *A second order dispersive FDTD algorithm for transverse electric Maxwell's equations with complex interfaces*, Computers and Mathematics with Applications **71**, 1010–1035 (2016).